Grid Anisotropy Reduction Method for Cellular Automata based Solidification Models

Ashish Arote[a,*], Junji Shinjo[a], D. Graham McCartney[b], Roger C. Reed[b,c]

[a] *Next Generation Tatara Co-Creation Centre (NEXTA), Shimane University, 1060 Nishikawatsu, Matsue 690-8504, Japan.*
[b] *Department of Materials, University of Oxford, Parks Road, Oxford, OX1 3PH, United Kingdom.*
[c] *Department of Engineering Science, University of Oxford, Parks Road, Oxford, OX1 3PJ, United Kingdom.*

Abstract

The reliability of a cellular automata (CA) simulation for a free dendritic growth problem relies heavily on its ability to reduce the artificial grid anisotropy. Hence, a computationally efficient, accurate and elegant cell capturing methodology is essential to achieve reliable results. Therefore, a novel cell capturing method termed *limited circular neighbourhood* (LCN) is proposed in the present study for solidification models. The LCN method is applied to the canonical test cases with an isotropic growth rate and is compared with other grid anisotropy reducing methods. It is observed that the LCN method is able to capture the growth orientation accurately. Moreover, the mass loss and shape error in the proposed method is significantly reduced as compared with the other methods. In addition, its performance is also evaluated for a free dendrite growth problem in a pure material in which the growth captured by the LCN method is found to be accurate. Finally, its efficacy is also demonstrated in the results presented for a constrained dendritic growth problem in a binary alloy with multiple growth sites.

Keywords: Grid anisotropy, cellular automata, solidification, dendrite

*Corresponding author at: Next Generation Tatara Co-Creation Centre (NEXTA), Shimane University, 1060 Nishikawatsu, Matsue 690-8504, Japan.
E-mail address: arote@riko.shimane-u.ac.jp (A. Arote)

Nomenclature

T	Local temperature	(K)
T_m	Liquid bath temperature far from the dendrite	(K)
f_s	Solid fraction	
L	Latent Heat	(J/m^3)
C_l	Liquid solute concentration	$(\%wt)$
C_s	Solid solute concentration	$(\%wt)$
D_l	Liquid solute diffusion coefficient	(m^2/s)
D_s	Solid solute diffusion coefficient	(m^2/s)
C_l^*	Liquid solute concentration at solid-liquid interface	$(\%wt)$
C_s^*	Solid solute concentration at solid-liquid interface	$(\%wt)$
C_0	Initial liquid concentration	$(\%wt)$
k	partition coefficient	
m	Liquidus slope	$(K/\%wt)$
n_x, n_y	Interface normal components along x and y directions	
G	Interface growth rate	(m/s)
V_x, V_y	Interface growth velocity along x and y directions	(m/s)
$\mathcal{CT}$	Computational time	(s)
ρ	Density	(kg/m^3)
c_p	Specific heat	$(J/(m^3K))$
λ	Thermal conductivity	$(W/(mK))$
α	Thermal diffusivity	(m^2/s)
κ	Interface curvature	(m^{-1})
Γ	Gibbs-Thomson coefficient	(Km)
μ_T	Surface-tension anisotropy	$(m/(sK))$
μ_k	Kinetic anisotropy	$(m/(sK))$
θ	Grain orientation angle	
θ_1	Angle between interface and horizontal axis	
δ	Surface-tension anisotropy amplitude	
δ_k	Kinetic anisotropy amplitude	
ϵ	Shape error	
L_1	Volume error	

1. Introduction

The modelling of microstructure formation in solidifying metals and alloys is a fundamental and important problem in the field of materials science. The microstructure of a solid determines its eventual mechanical properties and therefore understanding the fundamental mechanisms of dendritic growth is essential to control the properties of a product. *Dendrites* are the most important features in the solidification process and the driving force for their

formation is the presence of a non-zero crystalline anisotropy at the solid-liquid interface [1].

Recent years have seen the development of many numerical formulations for modelling dendritic growth during solidification. Selection of an appropriate simulation methodology is affected by the availability of computational resources and desired results required through them. Therefore, methods such as, the *Monte Calrlo* (MC), *Phase Field* (PF) and *Cellular Automata* (CA) formulations are largely employed in the previous studies. The MC method is based on a stochastic model which uses random numbers and probability to solve solidification problems through the trial and error formulation [2, 3]. PF models assume a smooth transition of the PF variable across the interface which extends over several grid points. The PF is developed by minimising the potential function that depicts the physical behaviour [4, 5]. CA based methods demonstrate dendritic growth using cell *capturing* rules. Unlike the MC models, the CA models are based on deterministic physical models and unlike the PF method, CA models can maintain a sharp interface where the solid-liquid interface does not extend beyond one grid cell. This sharp interface capturing in the CA method also allows it to be more computationally efficient than PF models [6]. However, a significant drawback that CA models demonstrate is the artificial anisotropy which causes inaccuracies in the growth orientation.

The capture rules that govern the growth of the solidification interface in the CA method are based on the variation of physical parameters that govern the growth of the solid-liquid interface. This allows the efficient distinction and transition between different states (solid, liquid and their interface) of matter. Therefore, CA methods have been applied in various growth models for predictions which include: *tumour growth* [7, 8, 9], *epitaxial growth* [10, 11, 12], *urban growth* [13, 14] and *solidification in binary alloys* [15, 16, 17, 18]. These models, based on the physical laws, perform growth within the *interface* cells (*neighbourhood* of a solid cell). The *Neumann* and *Moore* cell neighbourhoods are typically employed in CA methods as demonstrated in Fig 1. The central blue computational cell represents a cell in the solid state which captures the immediate four cells in the *Neumann* neighbourhood, whereas it captures eight cells as an interface in the *Moore* neighbourhood. These capture rules demonstrate a major limitation of the CA approach, namely artificial (grid) anisotropy caused by the CA square grid. This artificial anisotropy results in a loss of initial grain orientation, and produces solid cells along the axes (using the Neumann rule) and the diagonal (using the Moore rule). Therefore, as the grid anisotropy overlays the physical anisotropy condition, the results obtained through CA methods can lack quantitative behaviour [19].

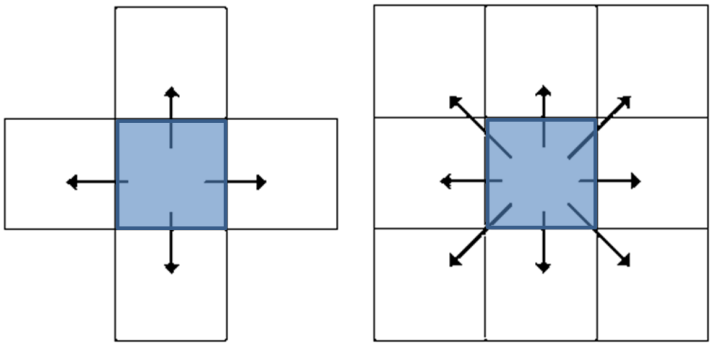

Figure 1: Interface cell configuration for a) Neumann and b) Moore neighbourhood.

Artificial anisotropy was also found to exist in the Monte Carlo model for dendritic growth, which references [20] and [21] attempted to amend using the uniform hexagonal grid system. Grid anisotropy can also lead to inaccuracies in some of the PF models [22]. However, Rappaz and Gandin [23] developed a *rectangular algorithm* that captures the set of rectangular interface cells only along the initial grain orientation. The algorithm requires vertex tracking of the growing polygon and re-initialisation of this polygon when the parent cell solidifies. Hence, the algorithm becomes complex and tedious to implement in three dimensions. Therefore, Gandin and Rappaz [24] improved the previous algorithm to a *de-centred square algorithm* but likewise the new algorithm too was not elegant enough to be implemented easily in three dimensions. Zhan et al. [25] attempted to further improve the *de-centred square algorithm* by using a multi-mesh layer, which they named as the limited angle method. The drawback of this method is its high computational cost. In the literature, stochastic approaches to reduce the grid anisotropy are also taken in the form of *zig-zag* and *random zig-zag* methods [26]. In these methods the fundamental capture rules such as *Neumann* and *Moore* are applied in an alternating manner to reduce the grid dominance. However, the results obtained through these methods demonstrate unphysical perturbations at the solid-liquid interface due to rule switching. Additionally, Wei et al. [27] also proposed a modified *Neumann* capturing rule where each cell in the *Neumann* neighbourhood was weighted based on the solid fraction to estimate its closeness to a solid-liquid interface. This method, called the *limited neighbour solid fraction* (LNSF) method, does well to reduce the grid anisotropy but does not remove it effectively enough. Grid anisotropy reduction was also achieved by modifying the amount of solute rejection in the diagonal cells of the *Moore neighbourhood* by Krane et al. [28]. As the *Moore neighbourhood* provides dominant growth along next nearest cells, the solute rejection is limited by a factor of 0.55 in these cells to reduce growth in them. A rotating grid technique was proposed by Liu et al. [29] where each grain is subjected to a grid rotated according to the grain orientation, and then it is made to expand up-to the global coordinates. This method is complicated to implement and even more complex for extension to three dimensional space. Furthermore, Marek [30] also developed an anisotropy reducing method namely *grid anisotropy reduction*

with diffusion (GARED) method. GARED established a diffused pilot field based on the solid state cells, and used it to produce a reduction parameter for growth velocity. As the additional diffusion field has to be computed, the computational efficiency is reduced. To the best of the authors' knowledge, at this point in time, the study on the improvement in capture rules has not led to further new rules being proposed. The most recent CA studies of solidification have employed the *de-centred square algorithm* [15, 16, 31], zigzag [32], and LNSF [33, 34] for microstructure modelling, whereas GARED has been used for meso-scale models [35]. However, as discussed earlier, quantitative information such as growth rate and orientation is affected significantly by the grid anisotropy in these methods and the simulation results need to be improved by reducing the grid dominance.

Therefore, the objective of the present paper is to report on the novel cell capturing method named *limited circular neighbourhood* (LCN) which removes the artificial anisotropy exerted on growing cells by a Cartesian square grid. Hence, through the canonical test cases it is established here that LCN is a computationally efficient, an elegant and an accurate cell capturing technique for obtaining reliable results from CA simulations. The LCN method makes use of the extended circular neighbourhood which allows the growth to be isotropic, and it is supported by a limiting parameter to maintain the interface smoothness. The foremost advantages that the new method provides are its simplicity, computational efficiency and effectiveness in reducing grid anisotropy.

2. Model description

The present work was aimed at modelling the growth of a solid-liquid interface in a solidification process, and the performance of the proposed method is evaluated here for the solidification test cases associated with isotropic and anisotropic growth. The solidification model is based on the *Cellular Automata (SA)* method. The new interface cells are *captured* based on the rules set by the specific CA method. The word *capture* here means marking/identifying the interface cells around a solidified (f_s) cell based on these rules. Once these cells are captured, the solid fraction is incremented in these cells based on the established solute and temperature fields.

2.1. Thermal field

The two dimensional transport of heat during solidification without convection is governed by Eq. 1.

$$\rho c_p \frac{\partial T}{\partial t} = \lambda \left[\frac{\partial^2 T}{\partial x^2} + \frac{\partial^2 T}{\partial y^2} \right] + \rho L \frac{\partial f_s}{\partial t} \tag{1}$$

Here, ρ, c_p, λ and L represent density, specific heat, thermal conductivity and latent heat of the melt, respectively; where temperature T evolves in time t within the domain $\Omega(x, y)$. It is assumed in the present study that these thermophysical properties are treated equivalent in solid and liquid regions. This simplifying assumption is commonly made in the literature as in references [31] and [36]. The second term on the right hand side of Eq. 1 denotes the latent heat of solidification that is released at the interface. Hence, the second term on the right hand side of Eq. 1 is evaluated only for the interface cells. The term f_s represents

the solid fraction inside a computational cell. The spatial discretisation is performed using the central difference scheme, whereas the temporal terms are resolved through the Crank-Nicholson method [37] (Appendix A).

2.2. Solute field

The solute or concentration field (C) is considered for a binary alloy melt or the melt consisting of more than one constituent. The solute transport for liquid and solid phases is governed by the Eqs. 2 and 3,respectively. The temporal terms of these equations are treated using Crank-Nicholson method [37] (Appendix A).

$$\frac{\partial C_l}{\partial t} = D_l \left[\frac{\partial^2 C_l}{\partial x^2} + \frac{\partial^2 C_l}{\partial y^2} \right] \tag{2}$$

$$\frac{\partial C_s}{\partial t} = D_s \left[\frac{\partial^2 C_s}{\partial x^2} + \frac{\partial^2 C_s}{\partial y^2} \right] \tag{3}$$

such that, C_l and C_s denote the liquid and solid solute concentrations, respectively. D_l and D_s represent the liquid and solid solute diffusivity, respectively. At the solid-liquid interface a local equilibrium is established as,

$$C_s^* = kC_l^* \tag{4}$$

$$C_l^* = C_0 + \frac{T^* - T_m + \Gamma\kappa\mu_T(\theta, \theta_1)}{m} \tag{5}$$

where, the terms with superscript * represent the solid-liquid interface values . The terms C_0, T_m, k, Γ, κ, m and $\mu_T(\theta, \theta_1)$ denote initial liquid concentration, bath temperature far from this interface, solute partition coefficient, Gibbs-Thomson coefficient, local interface curvature, liquidus slope of the phase diagram and surface-tension anisotropy, respectively. The surface-tension anisotropy is evaluated as $\mu_T = 1 + \delta cos(4[\theta - \theta_1])$, such that θ and δ are the grain orientation angle and anisotropy amplitude, respectively. The variable θ_1 is the angle between the interface and horizontal grid, and it is evaluated using interface normals (n_x, n_y) as $\theta_1 = tan^{-1}(n_y/n_x)$. The interface normals n_x and n_y are estimated using the Youngs' method [38]. Furthermore, the interface curvature κ is estimated according to reference [39].

2.3. Evaluation of growth in solid fraction

In a pure metal case the growth is driven by thermal, kinetic and curvature undercooling, whereas, for an alloy it is driven by the thermal, solutal, curvature and kinetic effects. Therefore, the growth in solid fraction for pure metal is estimated by Eq. 6 [30].

$$\Delta f_s = \frac{\Delta t}{\Delta x} G_p \tag{6}$$

$$G_p = (T^* - T_m) \cdot \mu_k(\theta, \theta_1) \tag{7}$$

where G_p denotes the growth velocity in pure metals and μ_k represents the kinetic anisotropy that is evaluated as $\mu_k = \mu_0 \left[1 + \delta_k cos(4[\theta - \theta_1])\right]$, with δ_k being the amplitude of kinetic

anisotropy. On the other hand, the growth rate in an alloy (G_a) is estimated through Eq. 8 [39].

$$\Delta f_s = \frac{\Delta t}{\Delta x} G_a \tag{8}$$

$$G_a = \left(V_x + V_y - V_x V_y \frac{\Delta t}{\Delta x} \right) \cdot \mu_k(\theta, \theta_1) \tag{9}$$

such that, V_x and V_x is the interface velocity components in x and y directions, respectively. The interface velocities V_x is estimated based on the [39] formulation as,

$$V_x = \frac{D_l}{\Delta x(1-k)} \left[\left(1 - \frac{C_{l_{i-1,j}}}{C_{l_{i,j}}} \right) (1 - f_{s_{i-1,j}}) + \left(1 - \frac{C_{l_{i+1,j}}}{C_{l_{i,j}}} \right) (1 - f_{s_{i+1,j}}) \right] + \frac{kD_s}{\Delta x(1-k)} \left[\left(1 - \frac{C_{s_{i-1,j}}}{kC_{l_{i,j}}} \right) f_{s_{i-1,j}} + \left(1 - \frac{C_{s_{i+1,j}}}{kC_{l_{i,j}}} \right) f_{s_{i+1,j}} \right] \tag{10}$$

The interface growth velocity in vertical direction (V_y) can be estimated in a similar manner.

2.4. LCN capture rule

The capture rule in CA method is required to identify the interface cells to carry-out the solidification in them. The proposed LCN method considers the circular neighbourhood (cell configuration) as demonstrated in Fig. 2. The black coloured cell at the centre represents a solid state cell and the surrounding red and blue cells denote the interface cells for the proposed method. The solid cell state here is identified by a maker as $I = 2$ and liquid cell state by $I = 0$; whereas interface cell by $I = 1$. All the red coloured cells are captured as the interface cells ($I = 1$) unconditionally when black cell becomes solid. On the other hand, the blue cells are captured conditionally and can be treated as an interface or a liquid cell ($I = 1 \vee 0$) depending on the satisfiability of inequality $\bar{f}_s > f_{LNSF}$. $\bar{f}_s$ is the average solid fraction in Moore neighbourhood, and f_{LNSF} is the value a priori choice. The proposed LCN method considers the extended circular neighbourhood of 20 cells in $2\mathcal{D}$ and 80 cells in $3\mathcal{D}$ coming under the outer white circle ($radius[R] = 2dx$), unlike Neumann and Moore neighbourhood which consider cells under the influence of circle $R = dx$. The growth in solid fraction (Δf_s) is carried out in the captured interface cells and is evaluated by Eqs. 6 and 8. As the radius of influence for the proposed method is twice ($R = 2dx$) the fundamental rule ($R = dx$), the growth rate (G_a or G_p) needs to be multiplied by a factor of 0.5 to make the method consistent. Hence the modified equation for the solid fraction growth becomes,

$$\Delta f_s = 0.5 \frac{\Delta t}{\Delta x} G \tag{11}$$

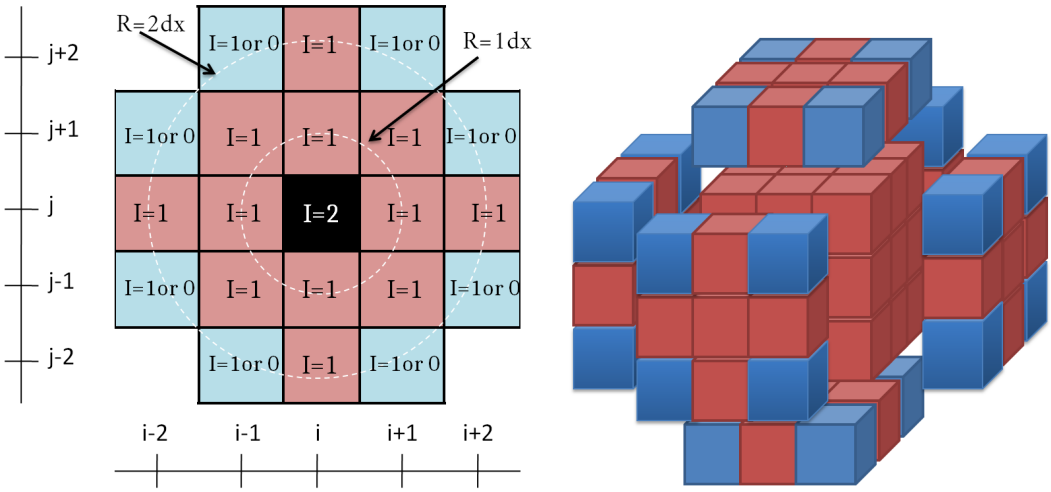

Figure 2: Limited circular neighbourhood (LCN) interface cell configuration in the a) two-dimensional ($2\mathcal{D}$) and b) three-dimensional ($3\mathcal{D}$) space.

The red cells are captured unconditionally and are treated as interface cells once the black cell is solidified. However, the blue cells in Fig. 2 are the interface cells which require the conditional capturing to reduce the shape error [40] of a growing interface. This conditional capturing is based on the *limited neighbour solid fraction* method [27] where the judgment is made about the closeness of these blue cells to a solid-liquid interface. A factor (f_{LNSF}) is a priori decided by carrying out the series of simulations for the equaixed dendrite case at different values of f_{LNSF}, and then an optimum value for which dendrite arms are both symmetric and consistent. This f_{LNSF} value will remain fixed for the particular material for an entire simulation. The average of solid fraction ($\bar{f}_s$) in *Moore* neighbourhood is carried out in $2\mathcal{D}$ as,

$$\bar{f}_s = \frac{1}{8}\sum_{i=1}^{8} f_{s_i} \tag{12}$$

where, f_{s_i} is the solid fraction in *Moore* neighbourhood. Therefore, in the present study, the blue cells are only captured when $\bar{f}_s > f_{LNSF}$. The simplified example of f_{LNSF} operation to decide the closeness of the blue cell to the interface is demonstrated in Fig. 3. In this example, the central red cell is about to become a solid cell ($f_s \to 1$) and will capture the neighbouring cells as interface cells. The blue-coloured cells will be captured (become interface cells) only if $\bar{f}_s > f_{LNSF}$. If two blue cells at the top are considered (*cell 1* and *cell 2*), then the average of solid fraction within a 3×3 cell stencil (orange for *cell 1* and green for *cell 2*) is performed using Eq. 12. This average is compared with f_{LNSF}. It can be observed that the $\bar{f}_s$ for *cell 1* is greater than $\bar{f}_s$ for *cell 2*. Therefore, *cell 1* has a greater possibility of being captured than *cell 2*. The *cell 2* is away from the interface and orientation axis as compared to *cell 1*. Hence, by following this methodology of cell capturing, it is evident that the growth is promoted along the orientation axis, reducing grid dominance.

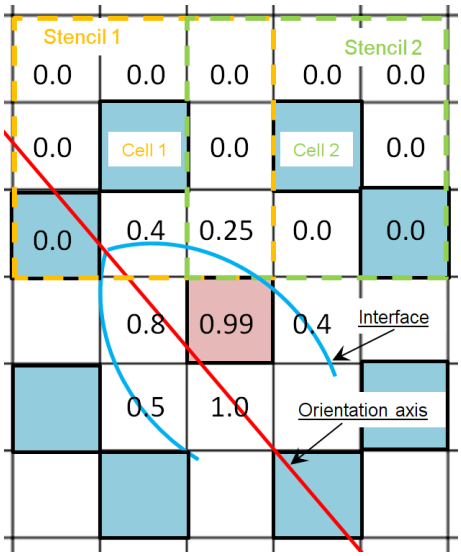

Figure 3: Schematic diagram to demonstrate working of $\bar{f}_s > f_{LNSF}$ inequality in Limited circular neighbourhood (LCN) interface cell configuration in the two-dimensional space. Red line denotes the grain orientation axis along which the dendrite is prescribed to grow.

To understand the solution procedure with LCN method better, the alloy solidification algorithm is demonstrated in Fig. 4. Initially, the solid seeds ($f_s = 1$) are initiated and marked as $I = 2$ and surrounding liquid region as $I = 0$. The interface cells are identified as $I = 1$ based on the LCN rules. In these interface cells the solidification velocities (V_x and V_y) are calculated and increase in the solid fraction is estimated using Eq. 10 and 8, respectively. The new temperature field is established over the entire domain through Eq. 1 and the solute field is estimated through Eq. 2-5 in the respective cells based on I value.

3. Numerical results

First, the present section provides a comparison between the proposed LCN method and the existing GARED [30], LNSF [27] and zig-zag [26] methods. This comparison is carried out for test cases of isotropic and anisotropic growth, and is based on the computational time, volume (ϵ) and shape (L_1) errors. The computational wall time ($\mathcal{CT}$) required for these tests is evaluated using `time.h` library of `C++`. The errors ϵ and L_1 are based on the solid fraction f_s and are estimated using Eqs. 13 and 14, respectively.

$$\epsilon = \frac{\sum |f_s^{predicted} - f_s^{exact}|}{\sum f_s^{extact}} \tag{13}$$

$$L_1 = \frac{\sum f_s^{predicted} - \sum f_s^{exact}}{\sum f_s^{extact}} \tag{14}$$

Secondly, we also report results for the LCN method when applied to the modelling of dendritic growth in the following environments: growth of a single isolated dendrite in an undercooled pure liquid; growth of a single isolated dendrite in an undercooled binary alloy; and constrained dendritic growth in a binary alloy from two nuclei.

```
Input: Thermal and solutal properties
Data: Initiate solid seeds (f_s = 1)
Input: Call solid cells as I = 2 and liquid as I = 0
while All I ≠ 2 do
    /* Identify states of each cell                                    */
    for All cells do
        Use LCN capture rule to identify cells as I = 1 (interface),
          I = 2 (solid) and I = 0 (liquid)
    /* Solidify interface cells                                        */
    for All cells do
        if I = 1 then
            Find V_x and V_y using Eq. 10      // Interface velocity components
            Solve Eq. 8
    /* Solve temperature equation                                      */
    for All cells do
        if I = 1 then
            Solve Eq. 1 with (L/c_p)(∂f_s/∂t)   // Add latent heat at the interface cells
        else
            Solve Eq. 1 without (L/c_p)(∂f_s/∂t)   // Solve for liquid and solid regions
    /* Solve solute equations                                          */
    for All cells do
        Calculate Curvature
        if I = 0 then
            Solve Eq. 2                    // Find solid solute concentration
        if I = 2 then
            Solve Eq. 3                    // Find solid solute concentration
        if I = 1 then
            Solve Eq. 4 and 5              // Find interface solute concentration
    for All cells do
        Update T, f_s, C_l and C_s
        Write data to a file and plot it
```

Figure 4: LCN alloy solidification code.

3.1. Isotropic growth test

The LCN method is evaluated for the outward and inward isotropic growth of solid respectively. The constant value for growth rate (G in Eqs. 6 and 8) of 0.01 is assumed for the present test. A domain of size 140×140 is resolved by a grid of 150×150 cells. The

outward growth test is performed by considering a circular solid nucleus of radius (R_1) 3 at the centre of the domain; whereas, for the inward growth test the solid region outside the circle of radius (R_2) 60 is considered as an initial state. Therefore, the exact radius of the solid-liquid interface after iterations i is $R_1 + 0.01i$ and $R_2 - 0.01i$ for outward and inward growth test, respectively.

Fig. 5 shows the comparison of the solid-liquid interface for the outward growth test. The central black circle denotes the initial solid nucleus of radius 3. It is observed that GARED provides more isotropy in growth which is evident from its circular interface topology. However, GARED shows an overestimation in solidification when compared to the exact solution (solid black circle). Furthermore, LNSF (with $f_{LNSF} = 0.375$) cannot maintain the isotropic growth and underestimates the solidification considerably. The zig-zag method is able to estimate the location of solidification interface accurately but the depicted interface itself is not smooth and contains unphysical perturbations. On the other hand, the proposed LCN method (with $f_{LNSF} = 0.165$) when compared with existing methods, predicts the solidification accurately. Fig. 5(c) demonstrates the $3\mathcal{D}$ results of solid fraction iso-surfaces ($f_s = 0.5$) obtained through $3\mathcal{D}$ LCN method as demonstrated in Fig. 2(b), and maintaining same earlier definition of simulation setup.

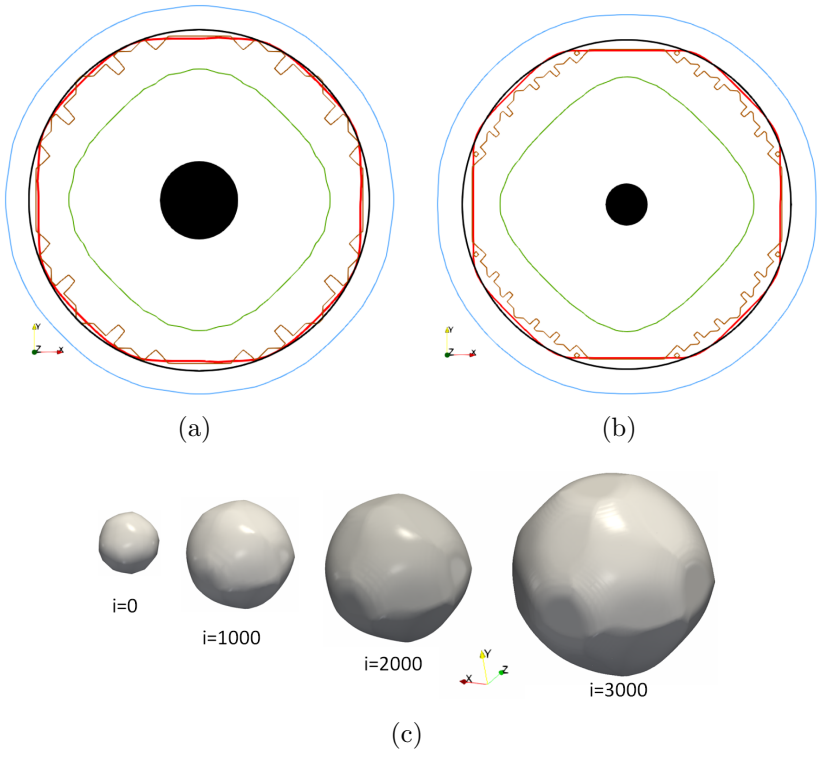

Figure 5: Results of the $2\mathcal{D}$ outward isotropic growth test and the comparison between LCN (red) and other methods (black: exact, blue: GARED, green: LNSF and brown: zig-zag) for the outward isotropic solidification after a) 1000 and b) 2000 iterations. Plot c) depicts $3\mathcal{D}$ solid fraction iso-surfaces ($f_s = 0.5$) obtained with the $3\mathcal{D}$ LCN method at various iterations (i).

The quantitative comparison between the various methods for the ϵ and L_1 errors along with their computational time ($\mathcal{CT}$) is reported in Table 1. It is observed that LCN method demonstrates the least loss in volume and conserves the solidification interface shape better than the other methods. It is observed that the computational efficiency for the LCN method is slightly more than LNSF method. This higher $\mathcal{CT}$ in LCN is due to its larger radius of influence. However, the computational cost is at par with these methods and in view of the growth accuracy, LCN proves to be a better method.

Table 1: Errors and $\mathcal{CT}$ values for various grid anisotropy reduction methods during outward growth test.

Method	$\epsilon(\%)$	$L_1(\%)$	$\mathcal{CT}(sec)$
		1000 iterations	
LCN	7.69	7.98	0.36
GARED	25.38	25.38	2.03
LNSF	48.34	48.34	0.33
zig-zag	11.15	11.15	0.37
		2000 iterations	
LCN	5.61	6.32	0.61
GARED	33.66	33.66	4.10
LNSF	49.00	49.00	0.58
zig-zag	12.36	12.36	0.65

The results for the isotropic inward growth test are shown in Fig. 6. It is observed through these comparisons that only the LCN and the zig-zag methods closely predict the exact solidification interface. However, the zig-zag method reveals the unphysical perturbations at the interface similar to those noted in the outward growth test. Whilst the GARED method shows a circular interface shape (isotropic growth), it overestimates growth considerably. Fig. 6(c) demonstrates the $3\mathcal{D}$ results of solid fraction iso-volume (grey) sliced by $yz - plane$ and liquid region (red) obtained through $3\mathcal{D}$ LCN method (Fig. 2(b)), and maintaining same earlier definition of simulation setup.

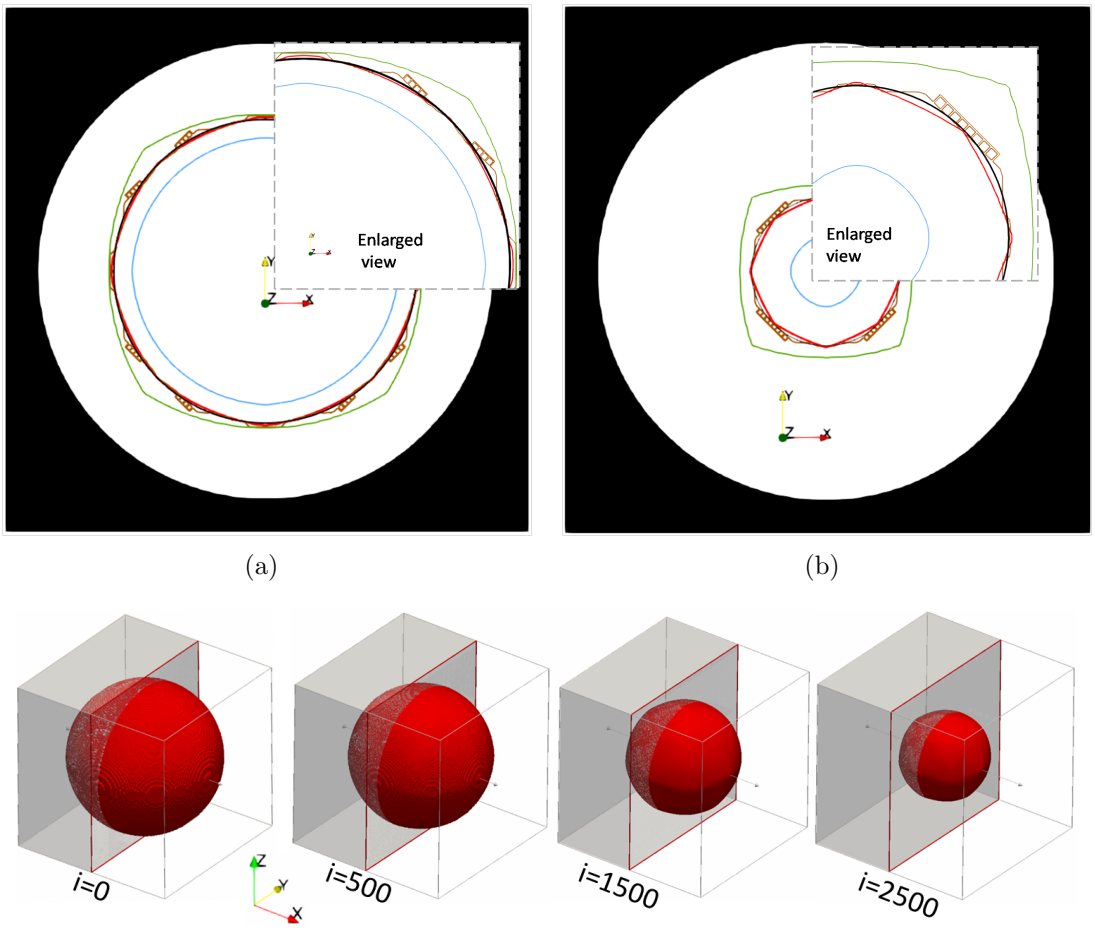

Figure 6: Results of the inward isotropic growth test the comparison between LCN (red) and other methods (black: exact, blue: GARED, green: LNSF and brown: zig-zag) for the inward isotropic solidification after a) 2000 and b) 4000 iterations. Plot c) depicts the sliced solid fraction by grey iso-volume and liquid by red iso-surface obtained from $3\mathcal{D}$ LCN method at various iterations (i).

The quantitative comparison between the various methods for the inward growth test is presented in Table 2. It is observed that the proposed LCN method demonstrates the least errors of all those considered. However, it has to be noted that, for the present test, LCN gives a higher computational time as compared to LNSF and zig-zag methods. This is due to the larger number of cells (20 in $2\mathcal{D}$) that the LCN method has to consider as compared with LNSF and zig-zag. However, the LCN method has the advantage of lower solidification errors and absence of unphysical interfacial perturbations.

Table 2: Errors and $\mathcal{CT}$ values for various grid anisotropy reduction methods during inward growth test.

Method	$\epsilon(\%)$	$L_1(\%)$	$\mathcal{CT}(sec)$
2000 iterations			
LCN	0.29	0.67	1.71
GARED	8.4	8.4	5.85
LNSF	4.77	4.77	1.43
zig-zag	0.49	1.04	1.28
4000 iterations			
LCN	0.51	0.67	3.28
GARED	5.45	5.45	11.63
LNSF	3.21	3.21	2.84
zig-zag	0.42	0.71	1.76

3.2. Anisotropic growth test

The ability of the proposed LCN method to capture the growth orientation accurately was evaluated through the anisotropic growth test described below. This test was carried out over the domain and grid resolution similar to § 3.1 with an initial circular solid nucleus of radius (R_i) 3 placed at centre of the domain. The growth rate (G in Eqs. 6 and 8) was 0.01, and the kinetic anisotropy $\mu_k = 1 + \delta_k cos(4[\theta - \theta_1])$ was provided with an amplitude (δ_k) of 0.2. Hence the change in solid fraction (Δf_s) is given as $\Delta f_s = (\Delta t/\Delta x) G\mu_k$.

Fig. 7 demonstrates the comparison of the anisotropic growth shown by various methods after 3000 iterations at θ of 22.5° and 30°. As the growth velocity is $G\mu_k$, the maximum growth should occur along the axis of orientation. Moreover, analytically, the radial distance covered by the solid-liquid interface along the orientation axis after N iterations at maximum anisotropy of $\mu_{k_{max}}$ is given by $R_i + G\mu_{k_{max}} N$. Therefore, the exact radial distance covered by the solidifying interface along the orientation axis after $N = 3000$ is 39. It is clearly revealed that the LCN method captures both the growth rate and orientation accurately. Whilst the LNSF method underestimates the growth, it is not able to capture the orientation effectively. The zig-zag method is able to capture the exact growth rate and the orientation satisfactorily, but the depicted interface is irregular due to spurious growth as discussed earlier. The GARED method overestimates the growth. and also shows a slight deviation (1°) in capturing the growth orientation as evident from the Fig. 7(b). It is also to be noted that this deviation is smaller for small θ values. Fig. 7(c) demonstrates the $3\mathcal{D}$ results of solid fraction iso-surfaces ($f_s = 0.5$) obtained through LCN method.

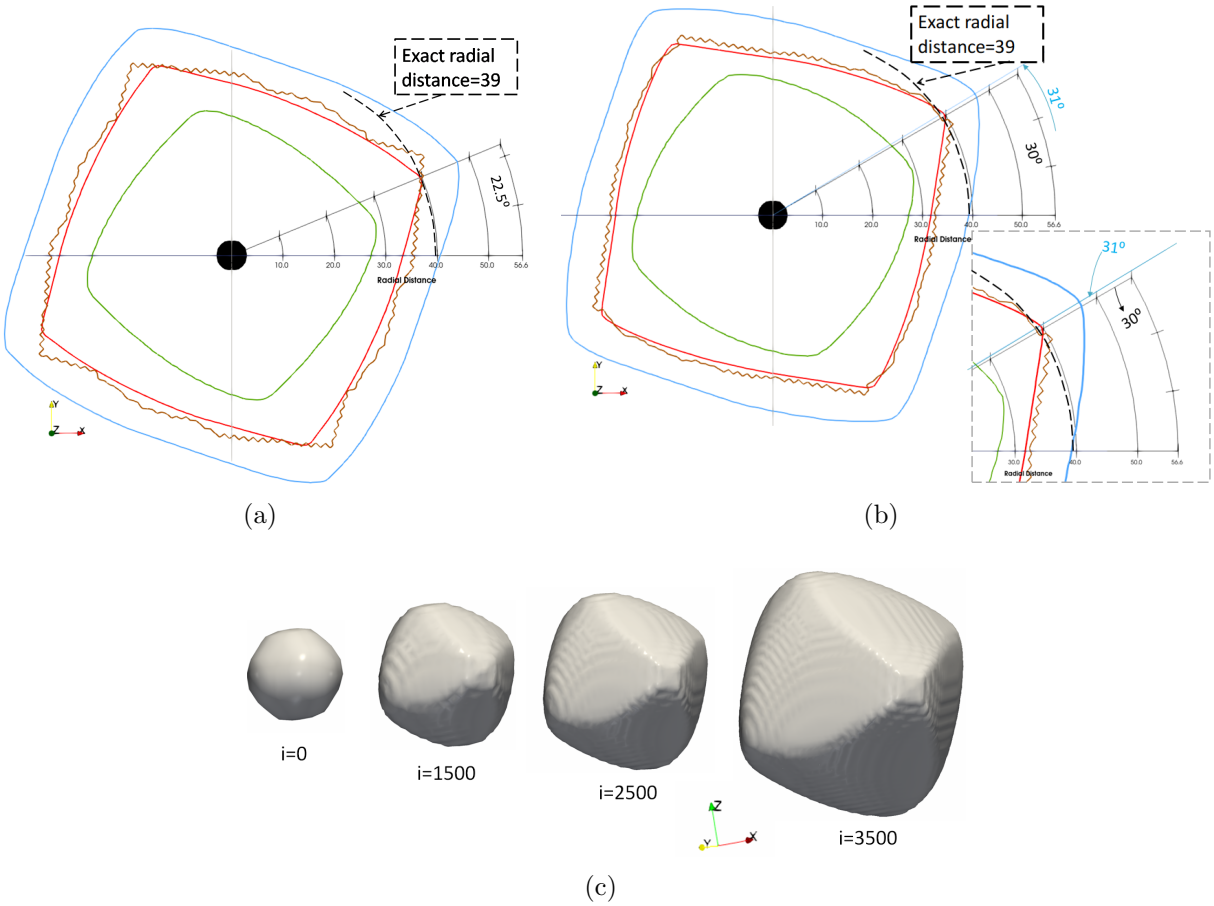

Figure 7: Results of the anisotropic growth test and the comparison between LCN (red) and other methods (black (dashed): exact growth extent, blue: GARED, green: LNSF and brown: zig-zag) for the anisotropy driven solidification after 3000 iterations at a) $\theta = 22.5°$ and b) $\theta = 30°$. Plot c) depicts solid fraction iso-surfaces ($f_s = 0.5$) obtained from $3\mathcal{D}$ LCN method (Fig. 2(b)) at various iterations (i).

3.3. Free dendritic growth in a pure metal

The dendrite formation test in a solidifying pure metal is carried out to evaluate the performance of the LCN method in a realistic physical growth process. The dendrite test is carried out based on the work of Marek [30], and the physical parameters used for the pure metal are listed in Table 3. The domain of 400 $\mu m \times$ 400 μm is resolved by the uniform grid of 250 $\times$ 250 cells for the present problem. The circular solid nucleus of radius equal to 3 grid cells is initialised. The domain which is initially at a bath temperature (T_m) which is cooled gradually at the circular boundary of radius 200 μm by temperature $T = T_m - 0.1t$. This condition is provided to the circular boundary to obtain uniform growth. Therefore, the growth in solid fraction is governed by Eqs. 6 and 7. Although, the *Gibbs-Thomson* coefficient needs to be considered in the dendrite formation [26], this parameter in [30] is presented in the form of anisotropy term. Therefore, in the present study to obtain a consistent comparison of results with Marek [30] a similar mathematical configuration is considered.

Table 3: Physical properties of the pure metal for the dendrite test [30].

Parameter	*Value*	*Unit*
ρ	$7{\times}10^3$	kg/m^3
λ	$3.5{\times}10^2$	$W/(mK)$
L	$2{\times}10^7$	J/m^3
c_p	$6{\times}10^6$	$J/(m^3K)$
T_m	1811	K
μ_0	10^{-3}	$m/(sK)$
δ_k	0.2	–

Fig. 8 demonstrates the evolution of the dendrite using the LCN method and its comparison with the other methods for the anisotropy angle of $\theta = 20°$. The LCN method (with $f_{LNSF} = 0.165$) captures the growth orientation well as compared to the GARED method as the latter shows a deviation of 3° whilst capturing the growth. It is to be mentioned here that the GARED method also shows broader dendrite arms as compared with the LCN method. This can be attributed to the overestimation of growth shown by GARED method which was discussed in the earlier sections. The LNSF value used for LCN method depends on the material configuration and is estimated through the numerical experiments for such configuration [27]. It is observed that LNSF method underestimates the growth and also deviates its orientation. The results for zig-zag method are not reported here as the results obtained through it were highly erroneous.

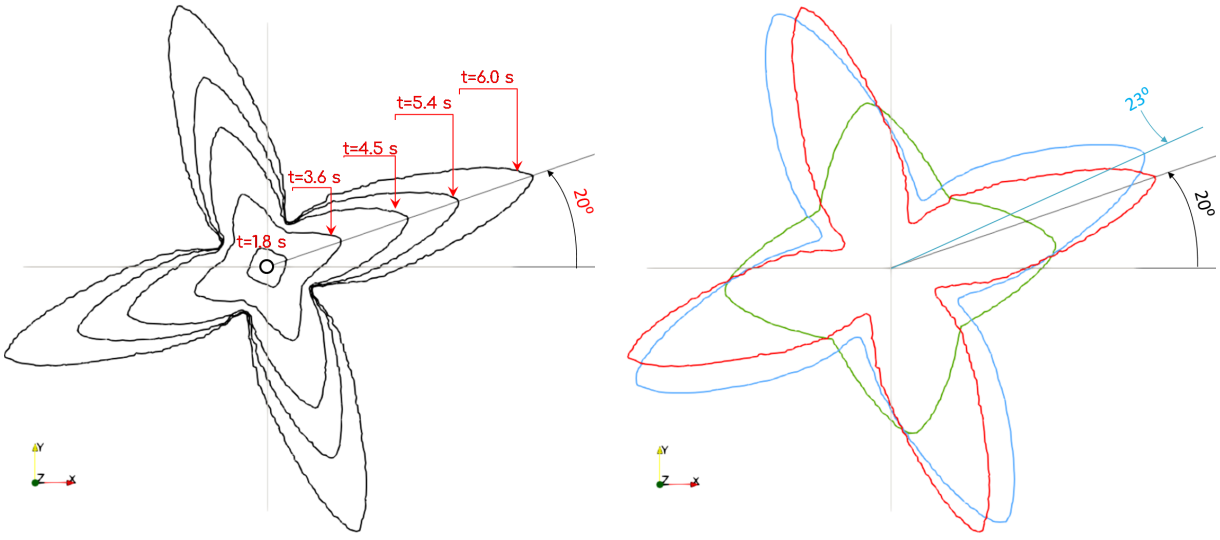

(a) (b)

Figure 8: Results of the pure metal dendrite growth for a) LCN method (at different time steps) and b) its comparison with other methods (red: LCN, blue: GARED and green: LNSF) at $\theta = 20°$.

The second (pure metal solidification) benchmark test is carried out to compare perfor-

mance of the proposed LCN method with the phase-field method. This test is governed by the non-dimensional version of Eq. 1, where temperature and temporal terms are scaled as $(T - T_m)/(L/c_p)$ and $t/(l^2/\alpha)$, respectively [41]. The numerical and model parameters used here for this test are based on Jokisaari et al. [41], and are chosen to examine sensitivity of the numerical model. Temporal and spatial discretization is based on the Euler and central difference method, respectively. The domain of 960×960 is resolved by 2400×2400 cells, and time step of 0.003 is used. The homogenous Neumann boundary condition is applied to all sides of the domain. Fig. 9(a) demonstrates the development of the solidification front over time, and temperature contours at $t = 1200$ are plotted. The interface topology obtained through different CA methods is compared with PF results from [41] in Fig. 9(b). It is observed that the CA methods are able to complete the growth of the dendrite arm equivalent to PF results at $t = 1200$ which PF required 1500 time units. This difference in the time scales arises due to the different growth velocities shown by both the methods, which can be attributed to the inherent formulations of these methods [6]. Moreover, the dendrite arm observed is more slender with a sharper tip in the CA results as compared to the PF results. This happens as fewer interface cells (characteristics of front-tracking methods) are present at the dendrite tip in CA method which produces the sharper dendrite tip, and this strong influence of the tip growth drives the dendrite arm to become slender [6]. The overall results depicted in Fig. 9(b) suggest that the CA methods are comparable to PF results, and are capable to effectively simulate dendrite growth even with the challenging parametric choices. Amongst the CA methods, as evident from the previous tests, GARED overestimates and LNSF underestimates the growth. As the grain orientation for the present test is $\theta = 0°$,

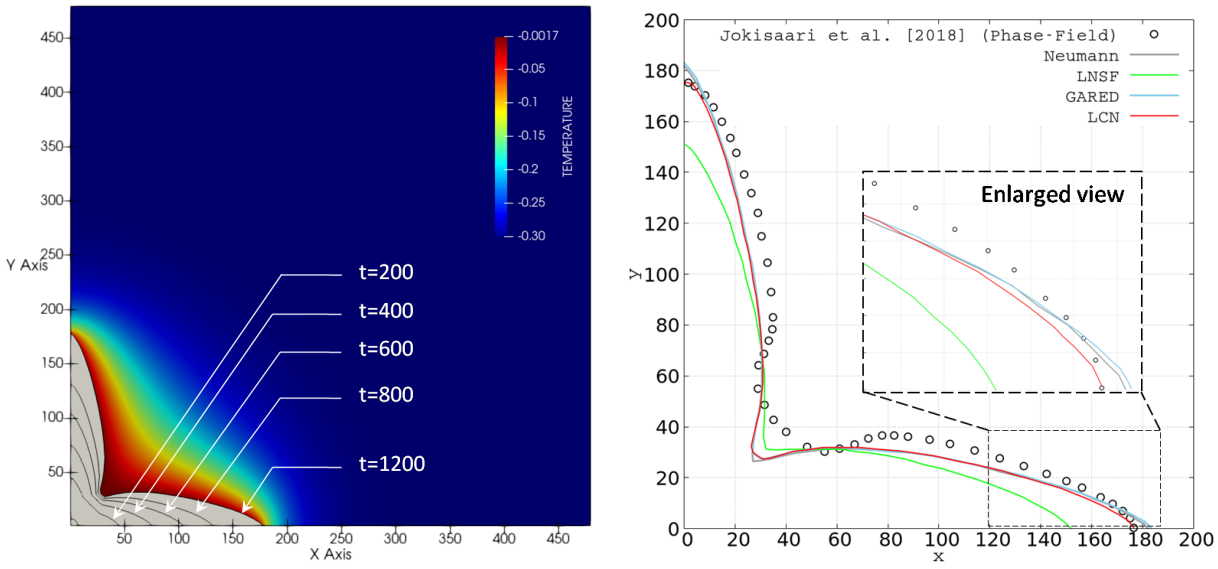

(a) (b)

Figure 9: Results of the pure metal dendrite growth for a) LCN method (at different time steps) and b) its comparison with phase-field ($t = 1500$) and other CA methods at $t = 1200$.

Neumann method should provide good results but it overestimates the growth; whereas

Moore and zig-zag method fail to obtain reasonable results (not shown in figure). However, the key point to note is that the LCN method provides good agreement with PF results and also has the capability to be used at arbitrary orientations and still obtain accurate results.

3.4. Free dendritic growth in an alloy

The LCN method is also applied to an alloy solidification problem to evaluate its performance. The Al-4wt%Cu alloy is considered for the present study and results are compared with those of Wei et al. [31]. The domain size of 300 $\mu m \times$ 300 μm is resolved by square cells of size 1 μm. The homogenous Neumann condition is imposed at the outer boundary of the domain. The circular solid nucleus of radius $3\Delta x$ (3 μm) is initiated at the centre of domain and a temperature under-cooling of 3 K is provided for this problem. The physical parameters employed for the Al-4wt%Cu alloy are listed in Table 4

Table 4: Physical properties of the Al-4wt%Cu [31] and Ni-4.85wt%Nb [36] alloy.

Parameter	$Value$		$Unit$
	$Al-4wt\%Cu$	$Ni-4.85wt\%Nb$	
ρ	2475	7491	kg/m^3
λ	30	25	W/(mK)
L	3.76×10^4	2.72×10^5	J/m^3
c_p	5×10^2	620	$J/(m^3K)$
T_m	919	1609	K
μ_0	1	1	$m/(sK)$
δ_k	0.6	0.6	–
δ	0.03	0.03	–
k	0.17	0.48	–
m	-3.39	-10.9	$K/wt\%$
D_l	3×10^{-9}	3×10^{-9}	m^2/s
D_s	3×10^{-13}	3×10^{-12}	m^2/s
Γ	2.4×10^{-7}	1.0×10^{-7}	Km

Fig. 10 depicts the Cu concentration and dendrite growth at an orientation angle $\theta = 22^\circ$. It is observed that the LCN method is able to capture the growth and its orientation satisfactorily. Moreover, the steady-state interface growth velocity of 40 $\mu m/s$, obtained through the present model is in agreement with results reported in reference [31]. It is observed that the initially high growth velocity continuously decreases to reach a steady state value. During growth solute is rejected at the solid-liquid interface and is diffused into the domain as discussed in reference [42]. This reduces the solute gradient across the interface which reduces the growth velocity and when this diffusion stabilizes in the domain, the growth velocity reaches a steady state.

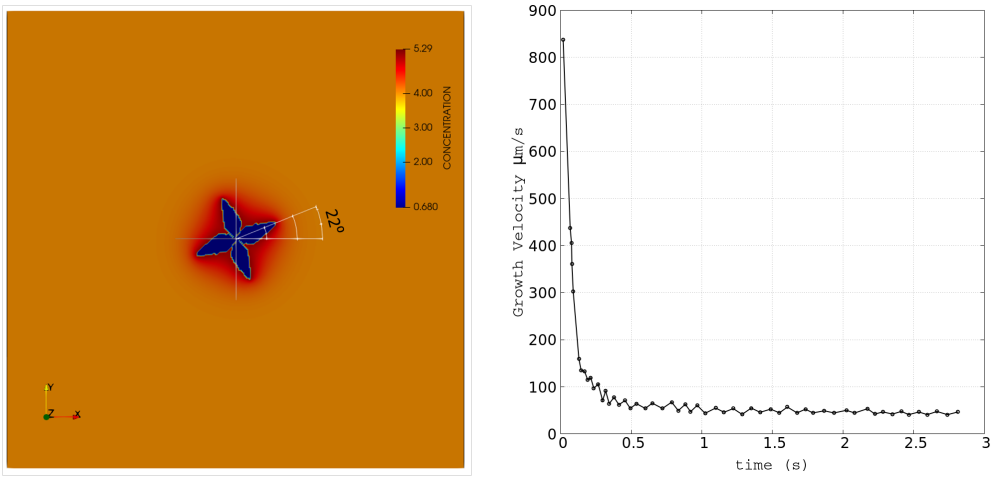

(a) (b)

Figure 10: An equiaxed dendrite develops for Al-4wt%Cu alloy. a) Cu concentration contours and b)plot of growth velocity versus time at $\theta = 22°$.

3.5. Constrained dendritic growth in an alloy

The comparison of constrained dendritc growth for Al-4wt% Cu and Ni-4.85wt% Nb alloys is performed to demonstrate the additional capability of the LCN method. The physical properties used for both these alloys are listed in Table 4. The simulation is performed within a domain of 150 $\mu m \times 150$ μm with a grid resolution of 350×350. As depicted in Fig. 11, initial seeds are placed on the bottom face at $L/4$ and $3L/4$ with orientation angle of 150° and 30°, respectively. The initial under-cooling of 3 K is provided within the domain. The directional cooling is imposed by the top face having the thermal gradient of 2000 K/m and this face is also gradually cooled further at a rate of 7 $Km^{-1}s^{-1}$. The other boundary faces of the domain are prescribed with homogenous Neumann condition.

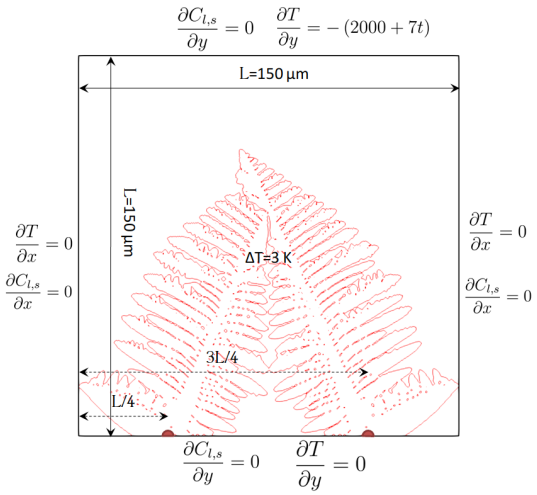

Figure 11: Computational domain and boundary conditions for the constrained dendritic growth problem.

Fig. 12 demonstrates the constrained dendrite growth results obtained through the LCN method for Al-4wt% Cu and Ni-4.85wt% Nb alloys. It is observed that the LCN method captures the growth orientation accurately. As the strong gradual cooling is provided by the top face, the contribution of thermal under-cooling $T_m - T$ becomes dominant over the solutal $m(C^* - C_0)$ and curvature $\Gamma\kappa\mu_T$ under-cooling. Hence, the primary dendrites oriented closer to the top face demonstrate accelerated growth than the other. It is observed that the Al-Cu alloy shows greater development of the lower primary and secondary dendrites as compared to the Ni-Nb alloy. Moreover, the Al-Cu alloy also shows the initiation of tertiary dendrites, which is subdued in the case Ni-Nb alloy.

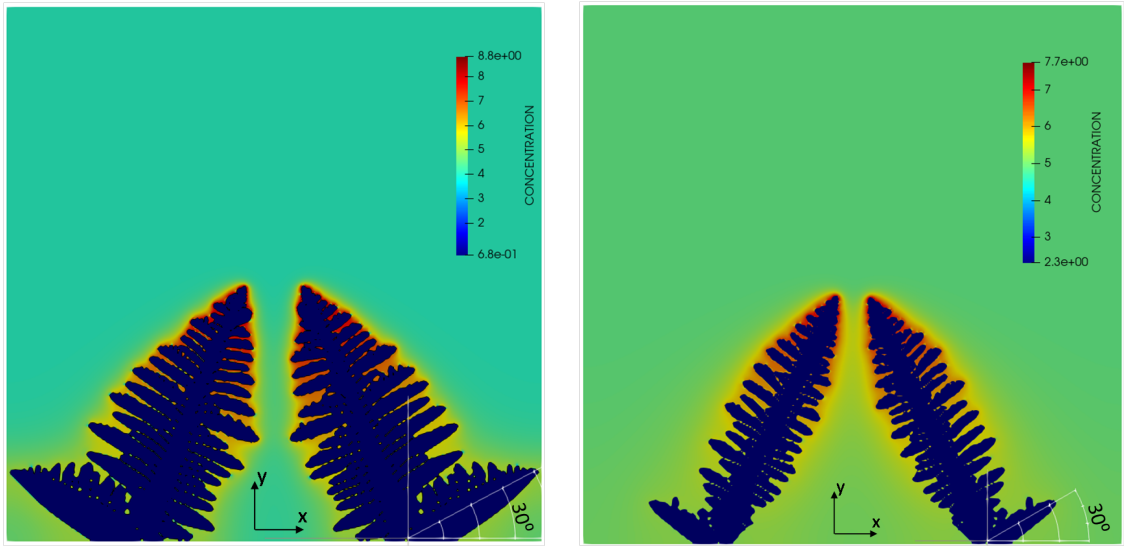

(a) (b)

Figure 12: Solute concentration contours for constrained dendrite growth in a) Al-4wt%Cu (at $t = 2.2$) and b) Ni-4.85wt%Nb (at $t = 3.9$) alloy.

Fig. 13 depicts variation of the temperature and solute concentration within the two alloys. This variation is evaluated across the lower primary dendrite tip along a segment (A-B) which is oriented towards the growth orientation axis ($\theta = 30°$). The lower primary dendrite is chosen for the comparison of these variables due to the distinct change in the growth rate of Al-Cu and Ni-Nb alloys as observed in Fig. 12. Fig. 13(a) demonstrates that the temperature gradient $T_m - T^*$ across the dendrite tip in Al-Cu alloy is greater than the Ni-Nb alloy. On the other hand, Fig. 13(b) demonstrates that the gradient of solute concentration $C^* - C_0$ in Al-Cu alloy is greater than Ni-Nb alloy. Therefore, as the contributions of thermal $T_m - T$ and solutal $m(C^* - C_0)$ under-cooling is higher in Al-Cu alloy as compared to Ni-Nb alloy, the growth velocity in Al-Cu is 154 $\mu m/s$, that is greater than Ni-Nb alloy growth rate which is 105 $\mu m/s$. Similar to the lower primary dendrite, the secondary dendrites in Al-Cu alloy also demonstrate accelerated growth than Ni-Nb alloy due to similar reasons discussed earlier.

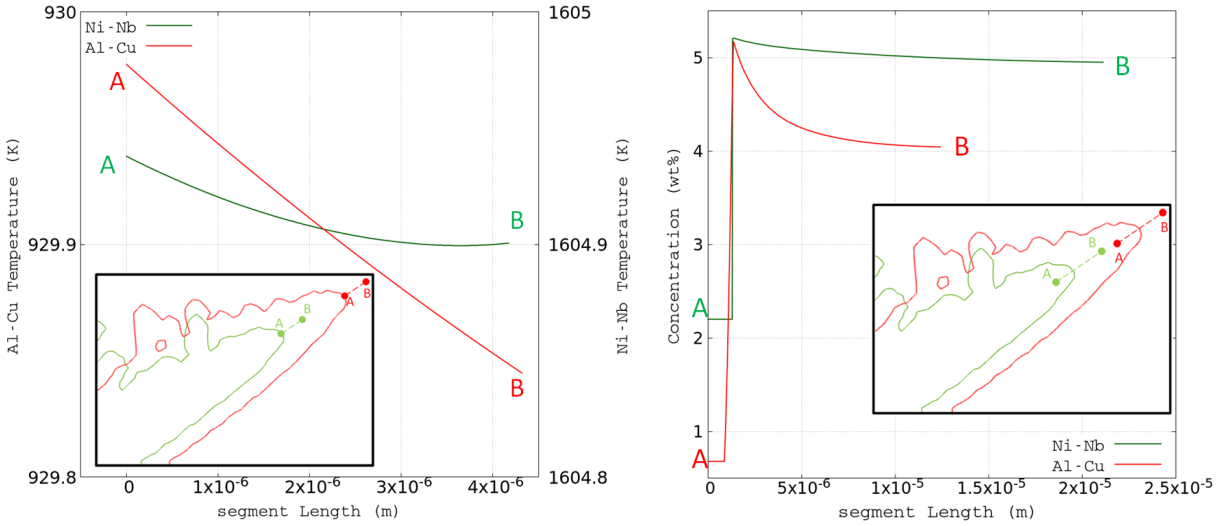

(a) (b)

Figure 13: Comparison between Al-4wt%Cu (red) and Ni-4.85wt%Nb (green) alloy for the a) temperature and b) solute concentration across the tip of lower primary dendrite at $t = 1.16$.

4. Conclusions

The present study is aimed at introducing a novel cellular automata (CA) cell capturing method named *Limited Circular Neighbourhood* (LCN) targeted at modelling solidification processes. The proposed method is introduced to tackle the issues of grid dominance and growth inaccuracy. The method is evaluated on the basis of benchmark solidification test cases with isotropic and anisotropic growth rate. The LCN method is also compared with other CA methods, which were aimed to reduce grid anisotropy, and the phase field method. Furthermore, the binary alloy solidification results are also demonstrated in the present study to assert the effectiveness of the LCN method.

1. The test cases involving the isotropic and anisotropic growth demonstrated that LCN method is able to reduce grid anisotropy and capture growth rate effectively as compared to the existing grid dominance reducing methods.
2. The LCN method shows better computational efficiency than GARED method; however, the $\mathcal{CT}$ is slightly greater than, but comparable to, the LNSF and zig-zag methods. This is due to the greater radius of influence (20 cells in $2\mathcal{D}$ and 80 cells in $3\mathcal{D}$) used for the LCN method. However, the growth accuracy and growth rate indicated by LCN method remains significantly better than these methods.
3. The LCN method is based on simplified cell capturing rules and can be elegantly implemented for the solidification problems.
4. Results obtained through the LCN method are comparable to phase field results. It requires less growth time in the CA-LCN method to reach an equivalent dendrite length than the PF method due to different growth velocities. Moreover, the dendrite arm

385 developed through LCN is more slender than the PF results due to the effect of a
386 sharper dendrite tip in LCN method.
387 5. The proposed method also provides accurate results when employed to the binary
388 metal alloy solidification problem.

CRediT author statement

Ashish Arote: Methodology, Formal analysis, Conceptualization, Investigation, Writing-Original Draft. **Junji Shinjo:** Conceptualization, Supervision, Writing Review and Editing, Funding acquisition, resources. **D. Graham McCartney:** Supervision, Writing Review and Editing. **Roger C. Reed:** Supervision, Writing Review and Editing.

Acknowledgement

This work was supported by Next Generation TATARA Project sponsored by the Government of Japan and Shimane Prefecture. Authors also want to thank **Dr. Yuanbo T. Tang**, Department of Materials, University of Oxford, Parks Road, Oxford, OX1 3PH, United Kingdom for his valuable comments for improving the present work.

Data Availability

The data that support the findings of this study are available from the corresponding author upon reasonable request.

Appendix A. Discretization using Crank-Nicholson (CN) method

The temporal term in temperature and solute transport equations are discretized using CN method. The temporal discretization is performed as follows for an arbitrary scalar $\mathcal{P}$ with its spatial diffusivity represented by $\mathcal{D}_p$,

$$\frac{\mathcal{P}_{ij}^{*}-\mathcal{P}_{ij}^{n}}{\Delta t}=\mathcal{D}_p\left[\frac{\mathcal{P}_{i+1,j}^{n}+\mathcal{P}_{i-1,j}^{n}-2\mathcal{P}_{ij}^{n}}{\Delta x^2}+\frac{\mathcal{P}_{i,j+1}^{n}+\mathcal{P}_{i,j-1}^{n}-2\mathcal{P}_{ij}^{n}}{\Delta y^2}\right] \tag{A.1}$$

$$\begin{aligned}\frac{\mathcal{P}_{ij}^{n+1}-\mathcal{P}_{ij}^{n}}{\Delta t}=&\frac{\mathcal{D}_p}{2}\left[\frac{\mathcal{P}_{i+1,j}^{n}+\mathcal{P}_{i-1,j}^{n}-2\mathcal{P}_{ij}^{n}}{\Delta x^2}+\frac{\mathcal{P}_{i,j+1}^{n}+\mathcal{P}_{i,j-1}^{n}-2\mathcal{P}_{ij}^{n}}{\Delta y^2}\right]\\&+\frac{\mathcal{D}_p}{2}\left[\frac{\mathcal{P}_{i+1,j}^{*}+\mathcal{P}_{i-1,j}^{*}-2\mathcal{P}_{ij}^{*}}{\Delta x^2}+\frac{\mathcal{P}_{i,j+1}^{*}+\mathcal{P}_{i,j-1}^{*}-2\mathcal{P}_{ij}^{*}}{\Delta y^2}\right]+\mathcal{S}\end{aligned} \tag{A.2}$$

$\mathcal{S}$ denotes the source term in the $\mathcal{P}$ transport equation.

References

[1] W. Kurz and D. J. Fisher, *Fundamentals of Solidification*. Trans Tech Publications Ltd., 1992.

[2] J. K. Mason, J. Lind, S. F. Li, B. W. Reed, V. V. Bulatov, and M. Kumar, "Kinetics and anisotropy of the monte carlo model of grain growth," *Acta Materialia, vol. 82, na, January 1, 2015, pp. 155-166.* [Online]. Available: https://www.osti.gov/biblio/1169883

[3] C. Krner, M. Markl, and J. Koepf, "Modeling and simulation of microstructure evolution for additive manufacturing of metals: A critical review," *Metallurgical and Materials Transactions A*, vol. 51, pp. 155–166, 2015.

[4] T. Takaki, "Phase-field modeling and simulations of dendrite growth," *ISIJ International*, vol. 54, no. 2, pp. 437–444, 2014.

[5] S. Kavousi and M. Asle Zaeem, "Quantitative phase-field modeling of solute trapping in rapid solidification," *Acta Materialia*, vol. 205, p. 116562, 2021. [Online]. Available: https://www.sciencedirect.com/science/article/pii/S135964542030999X

[6] A. Choudhury, K. Reuther, E. Wesner, A. August, B. Nestler, and M. Rettenmayr, "Comparison of phase-field and cellular automaton models for dendritic solidification in alcu alloy," *Computational Materials Science*, vol. 55, pp. 263–268, 2012. [Online]. Available: https://www.sciencedirect.com/science/article/pii/S092702561100680X

[7] A. Monteagudo and J. Santos, "Treatment analysis in a cancer stem cell context using a tumor growth model based on cellular automata," *PLOS ONE*, vol. 10, no. 7, pp. 1–16, 07 2015. [Online]. Available: https://doi.org/10.1371/journal.pone.0132306

[8] P. Gerlee and A. Anderson, "An evolutionary hybrid cellular automaton model of solid tumour growth," *Journal of Theoretical Biology*, vol. 246, no. 4, pp. 583–603, 2007. [Online]. Available: https://www.sciencedirect.com/science/article/pii/S0022519307000549

[9] D. Kawahara, Y. Nagata, and Y. Watanabe, "Improved cellular automata model shows that indirect apoptotic cell death due to vascular damage enhances the local control of tumors by single fraction high-dose irradiation," *Biomedical Physics & Engineering Express*, vol. 8, no. 1, p. 015028, 12 2021. [Online]. Available: https://doi.org/10.1088/2057-1976/ac4466

[10] R. Backofen and A. Voigt, "A cellular automata algorithm for step dynamics in continuum modeling of epitaxial growth," *Journal of Crystal Growth*, vol. 303, no. 1, pp. 100–104, 2007, proceedings of the Fifth Workshop on Modeling in Crystal Growth. [Online]. Available: https://www.sciencedirect.com/science/article/pii/S0022024806016125

[11] R. Kosturek and K. Malarz, "New cellular automaton designed to simulate epitaxial films growth," *Physica A: Statistical Mechanics and its Applications*, vol. 345, no. 3, pp. 538–546, 2005. [Online]. Available: https://www.sciencedirect.com/science/article/pii/S0378437104010805

[12] A. R. Ansari Dezfoli, Y. Lo, and M. M. Raza, "Prediction of Epitaxial Grain Growth in Single-Track Laser Melting of IN718 Using Integrated Finite Element and Cellular Automaton Approach," *Materials*, vol. 14, no. 18, p. 5202, 2021.

[13] Y. Chen, "An extended patch-based cellular automaton to simulate horizontal and vertical urban growth under the shared socioeconomic pathways," *Computers, Environment and Urban Systems*, vol. 91, p. 101727, 2022. [Online]. Available: https://www.sciencedirect.com/science/article/pii/S0198971521001344

[14] M. M. Aburas, Y. M. Ho, M. F. Ramli, and Z. H. Ashaari, "The simulation and prediction of spatio-temporal urban growth trends using cellular automata models: A review," *International Journal of Applied Earth Observation and Geoinformation*, vol. 52, pp. 380–389, 2016. [Online]. Available: https://www.sciencedirect.com/science/article/pii/S0303243416301143

[15] M. Rolchigo and R. LeSar, "Application of alloy solidification theory to cellular automata modeling of near-rapid constrained solidification," *Computational Materials Science*, vol. 163, pp. 148–161, 2019. [Online]. Available: https://www.sciencedirect.com/science/article/pii/S0927025619301417

[16] Y. Zhang, J. Zhou, Y. Yin, X. Shen, and X. Ji, "Multi-gpu implementation of a cellular automaton model for dendritic growth of binary alloy," *Journal of Materials Research and Technology*,

vol. 14, pp. 1862–1872, 2021. [Online]. Available: https://www.sciencedirect.com/science/article/pii/S2238785421007560

[17] C. D. Ridgeway, C. Gu, and A. A. Luo, "Predicting primary dendrite arm spacing in alsimg alloys: Effect of mg alloying," *Journal of Materials Science*, vol. 54, no. 13, p. 99079920, 2019.

[18] J. Kubo, Y. Koizumi, T. Ishimoto, and T. Nakano, "Modified cellular automaton simulation of metal additive manufacturing," *Materials Transactions*, vol. 62, no. 6, pp. 864–870, 2021.

[19] J. Strickland, B. Nenchev, and H. Dong, "On directional dendritic growth and primary spacinga review," *Crystals*, vol. 10, no. 7, 2020. [Online]. Available: https://www.mdpi.com/2073-4352/10/7/627

[20] M. P. Anderson, G. S. Grest, and D. J. Srolovitz, "Computer simulation of normal grain growth in three dimensions," *Philosophical Magazine B*, vol. 59, no. 3, pp. 293–329, 1989. [Online]. Available: https://doi.org/10.1080/13642818908220181

[21] J. Spittle and S. Brown, "Computer simulation of the effects of alloy variables on the grain structures of castings," *Acta Metallurgica*, vol. 37, no. 7, pp. 1803–1810, 1989. [Online]. Available: https://www.sciencedirect.com/science/article/pii/0001616089900655

[22] E. Miyoshi, T. Takaki, M. Ohno, and Y. Shibuta, "Accuracy evaluation of phase-field models for grain growth simulation with anisotropic grain boundary properties," *ISIJ International*, vol. 60, no. 1, pp. 160–167, 2020.

[23] M. Rappaz and C. A. Gandin, "Probabilistic modelling of microstructure formation in solidification processes," *Acta Metallurgica Et Materialia*, vol. 41, no. 2, pp. 345–360, 1993.

[24] C.-A. Gandin and M. Rappaz, "A 3d cellular automaton algorithm for the prediction of dendritic grain growth," *Acta Materialia*, vol. 45, no. 5, pp. 2187–2195, 1997. [Online]. Available: https://www.sciencedirect.com/science/article/pii/S1359645496003035

[25] X. Zhan, Y. Wei, and Z. Dong, "Cellular automaton simulation of grain growth with different orientation angles during solidification process," *Journal of Materials Processing Technology*, vol. 208, no. 1, pp. 1–8, 2008. [Online]. Available: https://www.sciencedirect.com/science/article/pii/S092401360800006X

[26] L. Wei, X. Lin, M. Wang, and W. Huang, "A cellular automaton model for the solidification of a pure substance," *Applied Physics A: Materials Science and Processing*, vol. 103, no. 1, pp. 123–133, 2011.

[27] W. Lei, L. Xin, W. Meng, and H. Weidong, "Orientation selection of equiaxed dendritic growth by three-dimensional cellular automaton model," *Physica B: Condensed Matter*, vol. 407, no. 13, pp. 2471–2475, 2012. [Online]. Available: http://dx.doi.org/10.1016/j.physb.2012.03.048

[28] M. Krane, D. Johnson, and S. Raghavan, "The development of a cellular automaton-finite volume model for dendritic growth," *Applied Mathematical Modelling*, vol. 33, pp. 2234–2247, 05 2009.

[29] Y. Liu, Q. Xu, and B. Liu, "Modified cellular automaton method for the modeling of the dendritic morphology of-binary alloys," *Tsinghua Science and Technology*, vol. 11, no. 5, pp. 495–500, 2006.

[30] M. Marek, "Grid anisotropy reduction for simulation of growth processes with cellular automaton," *Physica D: Nonlinear Phenomena*, vol. 253, no. October, pp. 73–84, 2013. [Online]. Available: http://dx.doi.org/10.1016/j.physd.2013.03.005

[31] J. Wei, X. Wang, and M. Yao, "Field variable diffusion cellular automaton model for dendritic growth with multifold symmetry for the solidification of alloys," *Modelling and Simulation in Materials Science and Engineering*, vol. 29, no. 7, p. 075005, 9 2021. [Online]. Available: https://doi.org/10.1088/1361-651x/ac1bf9

[32] W. Wang, Q. Shi, X. Zhu, and Y. Liu, "Numerical simulation of microstructure evolution in solidification process of ferritic stainless steel with cellular automaton," *Crystals*, vol. 11, no. 3, p. 309, 2021. [Online]. Available: https://www.mdpi.com/2073-4352/11/3/309

[33] J. Wang, R. Li, N. Li, W. Yan, W. Ma, and H. Chen, "Cellular automaton modeling of silicon facet formation during directional solidification," *Crystals*, vol. 8, no. 11, p. 399, 2018. [Online]. Available: https://www.mdpi.com/2073-4352/8/11/399

[34] W. Ma, R. Li, and H. Chen, "Three-Dimensional CA-LBM Model of Silicon Facet Formation during Directional Solidification," *Crystals*, vol. 10, no. 8, p. 669, 2020. [Online]. Available: https://www.mdpi.com/2073-4352/10/8/669

[35] J. Opara and R. Kuziak, "Study of phase transformations in complex phase steel using a mesoscale

cellular automaton model part i: Modeling fundamentals," *Journal of Metallic Materials*, vol. 72, pp. 17–31, 11 2020.

[36] L. Yuan and P. D. Lee, "Dendritic solidification under natural and forced convection in binary alloys: 2d versus 3d simulation," *Modelling and Simulation in Materials Science and Engineering*, vol. 18, no. 5, p. 055008, may 2010. [Online]. Available: https://doi.org/10.1088/0965-0393/18/5/055008

[37] J. Crank and P. Nicolson, "A practical method for numerical evaluation of solutions of partial differential equations of the heat-conduction type," *Mathematical Proceedings of the Cambridge Philosophical Society*, vol. 43, no. 1, p. 5067, 1947.

[38] D. L. Youngs, *Time-dependent multi-material flow with large fluid distortion.* Academic Press, 1982.

[39] L. Nastac, "Numerical modeling of solidification morphologies and segregation patterns in cast dendritic alloys," *Acta Materialia*, vol. 47, no. 17, pp. 4253–4262, 1999. [Online]. Available: https://www.sciencedirect.com/science/article/pii/S1359645499003250

[40] V. Boniou, T. Schmitt, and A. Vi, "Comparison of interface capturing methods for the simulation of two-phase flow in a unified low-mach framework," *International Journal of Multiphase Flow*, vol. 149, p. 103957, 2022. [Online]. Available: https://www.sciencedirect.com/science/article/pii/S0301932221003530

[41] A. Jokisaari, P. Voorhees, J. Guyer, J. Warren, and O. Heinonen, "Phase field benchmark problems for dendritic growth and linear elasticity," *Computational Materials Science*, vol. 149, pp. 336–347, 2018. [Online]. Available: https://www.sciencedirect.com/science/article/pii/S092702561830168X

[42] L. Beltran-Sanchez and D. Stefanescu, "A quantitative dendrite growth model and analysis of stability concepts," *Metallurgical and Materials Transactions A*, vol. 35, pp. 2471–2485, 01 2004.